

Submillimeter mapping and analysis of cold dust condensations in the Orion M42 star forming complex

X. Dupac ¹, M. Giard

Centre d'Étude Spatiale des Rayonnements (CESR)
9 av. du colonel Roche, BP4346, F-31028 Toulouse cedex 4, France

J.-P. Bernard, J.-M. Lamarre

Institut d'Astrophysique Spatiale (IAS)
Campus d'Orsay Bât. 121
15, rue Clémenceau, F-91405 Orsay cedex, France

C. Mény

CESR

F. Pajot

IAS

I. Ristorcelli, G. Serra ²

CESR

J.-P. Torre

Service d'Aéronomie du CNRS
BP3, F-91371 Verrières-le-Buisson cedex, France

Received _____; accepted _____

¹Send offprint requests to dupac@cesr.fr

²Guy Serra, principal investigator of the ProNaOS project, passed away on August the 15th 2000.

ABSTRACT

We present here the continuum submillimeter maps of the molecular cloud around the M42 Nebula in the Orion region. These have been obtained in four wavelength bands (200, 260, 360 and 580 μm) with the ProNaOS two meter balloon-borne telescope. The area covered is 7 parsecs wide (50 arcmin at a distance of 470 pc) with a spatial resolution of about 0.4 parsec. Thanks to the high sensitivity to faint surface brightness gradients, we have found several cold condensations with temperatures ranging from 12 to 17 K, within 3 parsecs of the dense ridge. The statistical analysis of the temperature and spectral index spatial distribution shows an evidence of an inverse correlation between these two parameters. Being invisible in the IRAS 100 μm survey, some cold clouds are likely to be the seeds for future star formation activity going on in the complex. We estimate their masses and we show that two of them have masses higher than their Jeans masses, and may be gravitationally unstable.

Subject headings: dust — infrared: ISM: continuum — ISM: clouds — ISM: individual (Orion Nebula)

1. Introduction

At about 470 pc, the Orion Nebula is one of the nearest massive star formation regions. It is part of the giant molecular complex of Orion, that has been revealed by the ^{12}CO maps of Kutner *et al.* (1977). The CO map of Maddalena *et al.* (1986) has shown the global distribution of gas in the Orion-Monoceros complex. This dense region of the interstellar medium, extending over approximately 30 degrees from southeast to northwest, is composed of several distinct areas. The most northern part is the gaseous region distributed on a circle around λ Orionis. To the south, the Orion Giant Molecular Clouds A and B extend over 15 degrees from north to south. To the southeast are located Monoceros and the Southern Filament. This set of giant molecular clouds is located 150 pc below the Galactic plane, and might have been formed by the collision of a cloud falling from the southern Galactic hemisphere onto the galactic disk (Franco *et al.* 1988). These molecular clouds are associated with large HII regions, the Orion Ia, Ib, Ic OB star associations, located on a 15 degree long ridge on the side away from the Galactic plane. The Orion Nebula is part of the Orion A giant molecular cloud, and its best studied region. Behind this H II region is the OMC-1 molecular cloud, which corresponds to a CO emission peak. This cloud is heated by the ultraviolet radiation of the OB stars of the Trapezium cluster (see for example Hillenbrand 1997). One can distinguish inside of OMC-1, two intense infrared sources: the punctual object of Becklin-Neugebauer (Becklin & Neugebauer 1967) and, 10 arcseconds to the south, the Kleinmann-Low Nebula (Kleinmann & Low 1967) that has an angular diameter of about 30 arcseconds. It is thought that BN is a young massive star ($25 M_{\odot}$) with an important mass loss. The first far infrared observation towards M42 has been performed by Low & Aumann (1970) in the spectral range from $30 \mu\text{m}$ to $1000 \mu\text{m}$. Then Harper (1974) mapped M42 at $90 \mu\text{m}$ and showed that the infrared emission originates from a more extended region. This area has been since intensively studied, from optical radiations to radio wavelengths (see for example the review of Genzel & Stutzki 1989). North from OMC-1, one can clearly see an extended "integral-shaped" filament (ISF hereafter) with two denser regions called OMC-2 and OMC-3 (see Bally *et al.* 1987). These cores have been studied both in molecular lines (recent studies of Dutrey *et al.* 1993,

Castets & Langer 1995, Nagahama *et al.* 1998) and continuum (recent works of Chini *et al.* 1997, Lis *et al.* 1998, Johnstone & Bally 1999). The 1300 μm maps of OMC-2 and OMC-3 of Chini *et al.* (1997) have shown the precise filamentary structure of these regions, studying several sources inside. On the dense ridge, the three cores OMC-1, OMC-2, OMC-3 have active star formation and seem to have been formed at roughly the same time. However there are important differences between them. OMC-1 has massive star formation and strong interactions between the gas and the infrared sources, increasing the gas temperature to ≈ 70 K, whereas OMC-2 is less luminous, contains low mass young stars and less energetic outflows than OMC-1. OMC-3 is thought to have a mass comparable to OMC-2 ($\approx 100 M_{\odot}$), but has less energetic outflows and lower gas temperature, suggesting that OMC-3 is less evolved than OMC-2, itself being less evolved than OMC-1 (see Castets & Langer 1995). The recent works in submillimeter continuum (Lis *et al.* 1998, Johnstone & Bally 1999) have high angular resolution, and thus have clearly shown the complex structure of the Orion Integral-Shaped Filament and discovered small condensations, as also did the ^{13}CO work of Nagahama *et al.* (1998) for the whole Orion A cloud. However the continuum ground-based observations do not have the sensitivity to map the weak emission from the dust away from the dense ridge. A recent far-infrared balloon-borne observation of Orion (Mookerjea *et al.* 2000) has derived the temperature distribution in Orion, the coldest source they found being 15 K.

We have observed this region with the submillimeter balloon-borne telescope ProNaOS, in order to better understand the variations of temperature and spectral index of the dust, and to study the cold phase of the dense interstellar medium. ProNaOS provides simultaneous measurements within four bands covering the wavelength range 200 μm - 800 μm , allowing to constrain both the temperature and the spectral index of the dust, in order to derive column densities and masses. The high sensitivity per beam allows us to study the extended emission of the dust, in and a few parsecs away from the dense ridge. A first ProNaOS mapping of OMC-1 and its surroundings has been analyzed by Ristorcelli *et al.* (1998). They discovered a cold (12.5 K) condensation and showed for four sources the variability of temperature and spectral index in the Orion Nebula complex. We present in this paper a detailed analysis of the submillimeter maps

obtained towards Orion with the second flight of ProNaOS in september 1996, at Fort-Summer, New Mexico. We have observed a much larger region than in Ristorcelli *et al.* including the integral-shaped filament and other cold clouds, two being seen for the first time in continuum emission. Section 2 deals with the observation performed, section 3 describes the maps obtained, and section 4 presents a detailed analysis of these maps.

2. Instruments and observations

2.1. Observations with ProNaOS

ProNaOS (PROgramme NAtional d’Observations Submillimétriques) is a French balloon-borne submillimeter experiment, with a 2 m diameter telescope (Buisson & Durand 1990). The main characteristics of the instrument are given in Table 1. The focal plane instrument SPM (Système Photométrique Multibande, see Lamarre *et al.* 1994) is composed of a wobbling mirror, providing a beam switching on the sky with an amplitude of about 6' at 19.5 Hz, and four bolometers cooled at 0.3 K. They measure the submillimeter flux in the spectral ranges 180-240 μm , 240-340 μm , 340-540 μm and 540-1200 μm , with sensitivity to low brightness gradients of about 1 MJy/sr in band 4. Thanks to an arrangement with dichroic filters, the measurement is performed simultaneously for all four bands on the same sky pixel. An off-axis star tracker and a 3-axis gyroscope allow to control the telescope pointing. Before a flight, the telescope and the whole payload are aligned and controlled. Two internal black bodies are calibrated with an absolute reference. They provide in-flight calibrations with an accuracy of about 5 % (relative), which has been checked against Saturn. The measurements on Saturn allow us to derive the beam shape up to a radius of six arcminutes from the axis. We use the integral of these beams to compare the Saturn measurement to the ground based calibration which is performed on extended blackbodies filling the beam. Regarding the ratio of the main central beam to the total beam, the beam efficiencies are from 0.78 in band 1 to 0.96 in band 4. This can be expressed as a mean wave-front error of about 15 μm . More details about the instrument can be found in Ristorcelli *et*

al. (1998).

The observing procedure is an altazimut scanning of the beam on the sky. The time-ordered data suffer thus from two main artifacts: the measured flux is differential, and the rotations of the telescope around the direction of observation distort the mapping pattern from a rectangular grid.

2.2. Data processing: a new method for ProNaOS data

The first processing applied to the data is correction from map distortion, taking into account the pointing of the telescope, including fine pointing errors due to the swinging of the gondola. Then usually the deconvolution method applied to ProNaOS data was EKH-like (Emerson *et al.* 1979) with a scan by scan filtering in Fourier space (see Sales *et al.* 1991). We have developed another method, based on direct linear inversion on the whole map, using a Wiener matrix. The Wiener filter (Wiener 1949) is the linear method that minimizes the reconstruction error. The restored sky map is computed as a linear expression of the data:

$$x_0 = Wy$$

x_0 being the reconstructed sky vector (i.e. the map), W the inversion matrix and y the signal vector. Assuming that the instrument is linear, the observation is:

$$y = Ax + n$$

where x is the true sky vector, A the observation matrix and n the noise vector. For W we use a Wiener matrix (see Tegmark 1997):

$$W = [S^{-1} + A^t N^{-1} A]^{-1} A^t N^{-1}$$

where S is the sky covariance matrix and N the noise covariance matrix. The convolution matrix A (point-spread function) takes into account the size and profile of the two beams, and the observing mode. In the case of the Orion region presented here, we have gathered two observation sequences. The first one is centered 10' north from BN/KL, and covers 50' by 40'. The second is offset to the west to map the edge of the molecular cloud, and covers about 30' by 20'. In

such data, one of the main problems encountered to properly reconstruct the maps, is the great contrast between the intense areas like OMC-1 and the weak areas, which are not less interesting. We have processed separately the second sequence, in order to decrease the contrast in these data and reconstruct precisely the intensities of the second sequence. The size of A is about 2000×3000 , which allows us to use a classical bi-conjugate gradient algorithm to invert the main term in W . The correlation matrices are estimated from the data, and can be refined with iterations and tests.

We show in Fig. 1 the map of the first sequence obtained with the EKH-like method, to be compared in Fig. 2 to the optimal maps obtained with the Wiener inversion method. Negative artifacts are clearly visible along the scans of the most intense area (along the elevation of OMC-1) with the EKH-like method, whereas they are significantly removed with the Wiener inversion method.

Fig. 1.— $200 \mu m$ map obtained with the EKH-like method (first observation sequence only). The color scale is logarithmic, and displays the positive reconstructed flux until 0.5 in log, then the light blue and the deep blue display the negative noise features, clearly visible along the elevation of OMC-1. The black lines in the color bar show the contour levels.

2.3. Observations with DiaBolo

Observations of Cloud 2 have been performed with the DiaBolo photometer at the focus of the IRAM 30 meter telescope in december 6/7 1996. DiaBolo is a two channel ($1200 \mu m$ and $2100 \mu m$) photometer which uses 100 mK bolometers. A detailed description of the instrumental setup can be found in Benoît *et al.* (2000). The configuration for the observation of Cloud 2 used one bolometer per wavelength channel with a beam size of about 30 arcseconds. We used the wobbling secondary mirror to subtract the background emission from the sky and the telescope. The wobbling amplitude was set to 120 arcseconds for a frequency of 0.8 Hz. We mapped a 6 by 6 arcminute area centered on the cloud by scanning the telescope beam in azimuth and elevation. The scanning speed was 6 arcsec per second, and the step between two lines was 15 arcseconds.

The maps were deglitched by filtering the signal of each scan using a temporal filter. After base line subtraction and rebinning of each scan, the dual beam maps were deconvolved from the beam switching using home-made IDL routines which follow the EKH method (Emerson *et al.* 1979).

3. Results

We present in Fig. 2 the images obtained in the two extreme photometric bands of ProNaOS-SPM. The noise level is about 4 MJy/sr rms in band 1 and 0.8 MJy/sr in band 4. However, due to the calibration uncertainty, the flux accuracy is not better than 5 % (1σ) relative between bands (10-20 % absolute).

Fig. 2.— ProNaOS maps in band 1 (200 μm , up) and band 4 (580 μm , bottom). For the band 1 image, we have merged the two sequences, reconstructed separately, into one image. The color scale is logarithmic, and displays the positive reconstructed flux until -1.5 in log, then the deeper blue and purple colors display the negative noise features. The noise level is about 4 MJy/sr rms in band 1 and 0.8 MJy/sr in band 4. However, due to the calibration uncertainty, the flux accuracy is not better than 5 % (1σ) relative between bands (10-20 % absolute). The black lines in the color bar show the contour levels. The black box drawn is the area mapped by Ristorcelli *et al.* (1998).

The brightest area observed is the molecular cloud OMC-1, which appears on our maps as a very intense region of thermal emission of the dust. Particularly in the area of BN/KL, the emission is very strong (it is the maximum of the submillimeter emission in this region): it reaches 49000 MJy/sr in band 1 (200 μm).

North from this intense central core is clearly visible a large molecular cloud extending over about 3 pc, called the integral-shaped filament, which presents an average spectral intensity at 200 μm of about 2300 MJy/sr.

One can see west from the central core a weaker condensation that we call Cloud 1, which has an intensity of 570 MJy/sr in band 1. A weaker emission can be seen around this cloud, which is

linked to the Cloud 2 northwards.

The Clouds 2, 3, 4 can be seen on the west of the maps in Fig. 2, from east to west. The Cloud 2 is a weak intensity condensation discovered during the first flight of ProNaOS (Ristorcelli *et al.* 1998). Its 200 μm intensity is 47 MJy/sr, but its maximum is closer to band 2 (260 μm), in which the spectral intensity reaches 50 MJy/sr.

The Clouds 3 and 4 are two extremely weak condensations. The 260 μm intensity of Cloud 3 is 32 MJy/sr, and the 200 μm intensity of Cloud 4 is 35 MJy/sr. These cold clouds, as well as Cloud 2, cannot be seen with IRAS 100 μm maps of the same region.

4. Analysis

4.1. Dust temperatures and spectral indexes

4.1.1. Derivation

To compare the emission obtained in the four submillimeter bands, and particularly to deduce emission spectra of the sources identified, it is necessary to degrade the angular resolution in all channels to the same beam. This is why we smooth the images in bands 1, 2, 3 with an adequate profile in order to obtain for each band the resolution of the fourth band (3.5'). The corresponding beams have been determined from the observation performed on the planet Saturn, considered as a reference point source.

The ProNaOS integrated fluxes in the four bands are given in Table 2. The integrated fluxes from other data (IRAS: <http://www.ipac.caltech.edu/ipac/iras/iras.html>, Harper 1974, Chini *et al.* 1984, Mezger *et al.* 1990, DiaBolo: Benoît *et al.* 2000) are given in Table 3.

We model the emission of the grains with a modified blackbody law:

$$I_{\nu fit}(\lambda, T, n) = C.B_{\nu}(\lambda, T).\lambda^{-\beta}$$

where λ is the wavelength, C a constant, T the temperature of the grains, β the spectral

Table 1: ProNaOS instrument characteristics

Primary mirror diameter	2045 mm, f/10			
Wobbling mirror	f=19.5 Hz, $\delta_{cross-elevation} = 6'$			
Pointing accuracy	20" absolute, 5" relative			
Band	1	2	3	4
(μm)	180 – 240	240 – 340	340 – 540	540 – 1200
Beam diameter (arcmin)	2	2	2.5	3.5
NEB ($MJysr^{-1}Hz^{-1/2}$)	22	26	8.5	5.3

Table 2: Integrated fluxes for ProNaOS data. The diameters of the regions are given in arcminutes.

	α_{1950}	δ_{1950}	$F_{\nu}(\text{Jy})$	$F_{\nu}(\text{Jy})$	$F_{\nu}(\text{Jy})$	$F_{\nu}(\text{Jy})$
	(h,min,sec)	($^{\circ},'$)	200 μm	260 μm	360 μm	580 μm
OMC-1(3.6')	5h 32min 38	-5 $^{\circ}$ 25'	28500 \pm 1400	14120 \pm 710	6010 \pm 300	1413 \pm 71
ISF						
(south) 5.4'	5h 32min 52	-5 $^{\circ}$ 13'	5130 \pm 260	3110 \pm 160	1489 \pm 74	404 \pm 20
ISF						
(north) 4.2'	5h 32min 38	-4 $^{\circ}$ 58'	2490 \pm 120	1449 \pm 72	699 \pm 35	182.9 \pm 9.1
Cloud1 (3.5')	5h 31min 30	-5 $^{\circ}$ 25'	461 \pm 23	308 \pm 15	209 \pm 10	51.0 \pm 2.6
Cloud2 (3.5')	5h 31min 16	-5 $^{\circ}$ 08'	37.9 \pm 1.9	41.0 \pm 2.0	27.0 \pm 1.3	9.95 \pm 0.50
Cloud3 (3.5')	5h 30min 15	-5 $^{\circ}$ 01'	25.0 \pm 1.3	25.8 \pm 1.3	15.26 \pm 0.76	5.82 \pm 0.29
Cloud4 (5.2')	5h 29min 11	-4 $^{\circ}$ 57'	63.2 \pm 3.2	59.5 \pm 3.0	21.5 \pm 1.1	12.54 \pm 0.63

index and B_ν the Planck function.

The three parameters C, T and β , are adjusted with a least square fit. Assuming optically thin emission (as did Ristorcelli *et al.* 1998), we can derive the optical depth $\tau_\nu = \frac{I_\nu}{B_\nu} = C.\lambda^{-\beta}$.

For some regions: Integral-Shaped Filament (south) and ISF (north), we include the IRAS 100 μm data in the fit. For the other regions, we cannot use these data, because they are either saturated (OMC-1), or drowned in the halo of OMC-1 (Clouds 1,2,3,4). For the fit of OMC-1, we included the 90 μm data of Harper (1974), the 1000 μm data of Chini *et al.* (1984), and the 1300 μm data of Mezger *et al.* (1990). These data have been averaged over the same beam diameter as ProNaOS, i.e. 3.5'.

For Cloud 2, we added the data obtained with the millimeter instrument DiaBolo at 1200 μm and 2100 μm . Three maps were repeated on Cloud 2, for a total observing time of about 1 hour. The values given in Table 3 have been obtained by integrating in a 3.5 arcmin circle centered on the cloud.

We give spectra of some regions in Fig. 3. The best parameters for each region selected are presented in Table 4.

4.1.2. Variations of the temperature and the spectral index

The dust temperature is highly variable all around this molecular complex: from **12 K** to **70 K**; and the spectral index changes much too: from **1.1** to **2.2**, as was also found for the four sources analyzed by Ristorcelli *et al.* (1998). The clouds separated from the denser regions (Clouds 3,4) are cold and have high indexes, but we can also see that some cold condensations (Cloud 1, 17 K, Cloud 2, 11.8 K) with high indexes can be close to the central region OMC-1 (1.5 pc). For the two sources in common (OMC-1 and Cloud 2), the parameters derived in this paper are well consistent with Ristorcelli *et al.* The spectral index derived for the OMC-1 cloud is 1.13 with quite small error bars, which is due to the high number of data points we have in the Rayleigh-Jeans tail of the dust emission, the temperature being around 70 K (see Ristorcelli *et al.* 1998 for a

Table 3: Integrated fluxes from other data. The approximative diameters of the regions are given in arcminutes.

	$F_\nu(\text{Jy})$	$F_\nu(\text{Jy})$	$F_\nu(\text{Jy})$	$F_\nu(\text{Jy})$	$F_\nu(\text{Jy})$	$F_\nu(\text{Jy})$
	90 μm Harper	100 μm IRAS	1000 μm Chini	1200 μm DiaBolo	1300 μm Mezger	2100 μm DiaBolo
OMC-1(3.6')	258000 ± 77000	—	480 ± 140	—	187 ± 56	—
ISF						
(south)	—	10600 ± 2600	—	—	—	—
ISF						
(north)	—	4000 ± 1000	—	—	—	—
Cloud2 (3.5')	—	—	—	0.77 ± 0.13	—	0.120 ± 0.030

Table 4: Temperature and spectral index from the fit of the spectra, optical depth. The error bars are given for 68 % confidence interval. The approximative diameters of the regions are given in arcminutes.

	T (K)	β	$\frac{\tau_\nu}{10^{-3}}$	$\frac{\tau_\nu}{10^{-3}}$
			200 μm	580 μm
OMC-1(3.6')	$66.1^{+10.2}_{-9.4}$	$1.13^{+0.06}_{-0.09}$	47 ± 6	10.4 ± 0.8
ISF				
(south) 5.4'	$22.4^{+2.1}_{-2.0}$	$1.71^{+0.12}_{-0.19}$	5.3 ± 1.0	1.3 ± 0.1
ISF				
(north) 4.2'	$25.2^{+2.5}_{-2.5}$	$1.68^{+0.13}_{-0.17}$	15 ± 3	1.9 ± 0.2
Cloud1 (3.5')	$17.0^{+3.4}_{-2.5}$	$2.21^{+0.23}_{-0.48}$	4.0 ± 3.2	0.76 ± 0.23
Cloud2 (3.5')	$11.8^{+0.6}_{-0.7}$	$2.20^{+0.15}_{-0.18}$	4.2 ± 1.5	0.43 ± 0.07
Cloud3 (3.5')	$13.3^{+2.6}_{-2.1}$	$1.98^{+0.39}_{-0.79}$	$1.4 < 4.2(3\sigma)$	0.19 ± 0.07
Cloud4 (5.2')	$16.9^{+7.3}_{-4.1}$	$1.91^{+0.00}_{-1.29}$	$0.5 < 2.1(3\sigma)$	0.12 ± 0.06

precise discussion on this region). For such a region, the submillimeter spectrum we observe could come from a mixture of several dust temperatures. It has been shown by Ristorcelli *et al.* (1998) that the cold dust column density required to explain the fit temperature (83 K) with $\beta = 2$ was 40 times more massive than the warm component. They concluded that the spectral index of the dominant component had to be around 1. The ISF extended emission is quite cold (22 K - south, 25 K - north) with spectral indexes of about 1.7. In this temperature range, the ProNaOS data points combined with the IRAS 100 μm point give quite small error bars. We have simulated a temperature distribution with $\beta = 2$, with a bell function around 17 K having a fwhm of about 9 K. This leads to fit the spectrum with a temperature of 21 K and a spectral index of 1.8. Thus the temperature and spectral index range we observe in the ISF could partly be explained by a distribution of temperatures with a colder central temperature, and a higher index. The clouds 1 and 2 have the highest spectral index we found in this region (2.2), Cloud 2 being the coldest (11.8 K), with error bars considerably reduced, thanks to the DiaBolo millimeter data, with respect to the parameters given in Ristorcelli *et al.* The Cloud 3 is another cold cloud (13.3 K) with a high index (1.98), however the error bar on the spectral index is large. The Cloud 4 has ill-defined parameters, but seems also to have comparable values of the temperature and the spectral index.

Recently, high angular resolution submillimeter maps of the integral-shaped filament have been obtained from the ground using the CSO at 350 microns (Lis *et al.* 1998) and the JCMT at 450 and 850 microns (Johnstone & Bally 1999). However, these maps do not include the fainter regions evidenced here (Clouds 1-4) nor the diffuse emission around the ISF that we show in this article. Comparing their maps to the ProNaOS ones, it is clear that the extended emission of the dust around the brightest sources is missed by these ground-based experiments. Combining their 350 μm map and the IRAM 1.3 mm map of Chini *et al.* (1997), Lis *et al.* derived a map of the dust emissivity index over the brightest region surrounding OMC-1, including Orion-S and the Orion bar. Under the assumption of a single dust temperature (55 K) over this region, they derived emissivity indexes in the range 1.3 to 2.7, the lower values being observed toward the Orion bar (about 1.7) and IRC2 (1.8) while higher values (typically 2.3) appear north of OMC-1. The index values they derived toward the brightest region of the map (IRC2 and Orion-S) is in

the range 1.8-2.0 when averaged within the beam size of our observations. Even if we take into account that the temperature they assumed is too low compared to the one we measure (66 K), these values remain clearly higher than the dust emissivity index value we derived for this region ($\beta=1.13$). This discrepancy may originate from their use of two distinct datasets with different systematic calibration errors.

4.2. Temperature - index inverse correlation

We have computed the 68 % (1σ) confidence likelihood contours of the (T, β) values for each cloud (see Fig. 4) -*N.B.*: the likelihood is proportional to $e^{-\frac{\chi^2}{2}}$.

The correlation coefficient between T and β has been computed globally for the studied regions. We have therefore seven couples (T, β) which correlation we analyse by:

$$C = \frac{\sum (T_i - \bar{T}) \cdot (\beta_i - \bar{\beta})}{\sqrt{\sum (T_i - \bar{T})^2 \cdot \sum (\beta_i - \bar{\beta})^2}}$$

A first analysis of the plot in Fig. 4 shows an inverse correlation between the temperature and the spectral index, which means that the regions of high index have the lowest temperature, and the regions of low index have the highest temperature. The correlation coefficient calculated is **-0.92**. This correlation is, for a part, dominated by the warm area of OMC-1, but the correlation coefficient is still **-0.83** when this area is not included.

One can see in Fig. 4 that the likelihood contours are banana-shaped, that is mainly due for OMC-1 to the insensitivity to temperature variations in the Rayleigh-Jeans tail, and for the cold clouds to the relatively bad sensitivity to spectral index variations, as we do not have millimeter data for most of them. However the fit procedure itself could induce an amount of inverse correlation between the temperature and the spectral index. To prove that this correlation is for the most part not due to the fit, we performed simulations. Repeated fits on noisy simulated data with no intrinsic (T, β) correlation show that the fitting procedure itself induces a correlation coefficient lesser in absolute than **-0.4**. This artifact of the fit is thus insufficient to explain the correlation found on real data.

Our conclusion is that this inverse correlation found between the temperature and the spectral index has to be an intrinsic physical property of the grains.

Laboratory experiments (see Agladze *et al.* 1996 and Mennella *et al.* 1998) showed this effect for temperatures down to 10 K, but it had never been systematically shown until now with observations. Agladze *et al.* (1996) measured absorption spectra of crystalline and amorphous grains between 0.7 and 2.9 mm wavelength. They deduced an inverse correlation between the power-law index β and the temperature in the temperature range 10-25 K, and attributed it to two level tunnelling processes. The measures of Agladze *et al.* are for us insufficient to justify our observation in the submillimeter spectral range, because absorption can be very different than in the millimeter range. Mennella *et al.* (1998) measured the absorption coefficient of cosmic dust analogue grains, crystalline and amorphous, between 20 μm and 2 mm wavelength, in the temperature range 24-295 K. They deduced an inverse correlation between T and β , and attributed it to two phonon difference processes.

4.3. Column densities

4.3.1. Derivation

To calculate the opacity of the grains, the masses and densities of the studied regions, we need to estimate the column density in each pixel of the maps, i.e. the mass of gas and dust along the line of sight. For this we use the dust 100 μm opacity from Désert *et al.* (1990). It allows us to estimate the column density from the spectral intensity. We consider only the thermal emission of the big grains, which dominate widely in this spectral range, and we assume that the spectral index does not change in the ProNaOS spectral range. We take into account the variability of the dust spectral index of the different regions. This gives us a simple self-consistent model that allows us to estimate the column density N_H , as a function of the spectral intensity and the spectral index. We adopt the value of the opacity $\kappa_{100\mu m} = 0.361 \text{ cm}^2/g$ (per gram of total medium: gas and dust) at 100 μm , because this value is well constrained from IRAS data. This is calculated

from the extinction curves given in Désert *et al.* The opacity κ is defined as $\frac{\tau}{N_H.m_H}$, thus the relation between the gas column density and the fit parameters is:

$$N_H = \frac{C.\lambda^{-\beta}}{\kappa.m_H}$$

where m_H is the proton mass and κ the gas and dust opacity.

Then for the Désert *et al.* value of $\kappa_{100\mu m}$ we have:

$$N_H = 1.67 \cdot 10^{24} \cdot C \cdot (100 \mu m)^{-\beta}$$

with N_H in protons/cm² and C in μm^β .

We make another simple model using the 100 μm opacity of the Ossenkopf & Henning (1994) model, which is specific to protostellar cores. The opacity introduced then is $\kappa_{100\mu m} = 1 \text{ cm}^2/g$. The proportionality relation is:

$$N_H = 6.02 \cdot 10^{23} \cdot C \cdot (100 \mu m)^{-\beta}$$

with N_H in protons/cm² and C in μm^β .

4.3.2. Analysis

We compare our column density results to those derived from observations of the rotational transition $J = 1 - 0$ of ^{13}CO , made by Nagahama *et al.* (1998). We transform the observed W_{13CO} into the column density in cm⁻² by using the correspondence established by Bally *et al.* (1991) in the Orion Nebula. This correspondence has been calculated using comparisons between the IRAS far-infrared dust emission and the CO lines in Orion. Ristorcelli *et al.* (1998) have taken for the BN/KL region the coefficient: $N_H/W_{13CO} = 2 \cdot 10^{21} \text{ cm}^{-2}/(\text{K km/s})$, assuming an excitation temperature of about 80 K. We have used the same value of this coefficient for estimating the column density of OMC-1 from the ^{13}CO data. For the cold and rather cold clouds we study in this article, we choose to adopt $N_H/W_{13CO} = 10^{21} \text{ cm}^{-2}/(\text{K km/s})$, as it is mentioned by Bally *et al.* (1991) for an excitation temperature of about 30 K. Indeed the ^{13}CO emission towards

the cold clouds we observe (< 20 K) is not likely to trace very well the clump itself, but rather the surrounding gas, which has probably a quite higher temperature. Recent CO observations of Ristorcelli *et al.* (2001, *in preparation*) of Cloud 2 seem to support this, as the ^{13}CO emission of this cloud is more diffuse than the C^{18}O emission. This method gives a simple way to estimate the gas column density from these ^{13}CO data. As we can see in Table 5, for OMC-1, ISF-N and ISF-S, there is a rather good agreement between N_H estimated from ProNaOS data by the model from Désert *et al.* and N_H from ^{13}CO data. Indeed, the $\frac{N_H^{dust}}{N_H^{13\text{CO}}}$ ratio is 1.3 for OMC-1, 0.9 for ISF south and 1.5 for ISF north. Of course the uncertainties on both values are large and difficult to estimate, but these results prove that these values found are quite robust. The cold clouds (1,2,3,4) have ^{13}CO column densities in rather good agreement with the ProNaOS Ossenkopf & Henning estimations: $\frac{N_H^{dust}}{N_H^{13\text{CO}}}$ is 0.7 for Cloud 1, 1.2 for Cloud 2, 1.7 for Cloud 3 and 2.4 for Cloud 4. This rather good agreement between the ^{13}CO estimated column densities and the O&H estimated ones may be explained by the fact that some cold condensations are the site of formation of molecular ice mantles on the grains, and of coagulation of grains. These processes are taken into account by the model of Ossenkopf & Henning. However, the ^{13}CO estimations for N_H seem under-estimated for Clouds 3 and 4, compared to the ProNaOS O&H values ($\frac{N_H^{dust}}{N_H^{13\text{CO}}}$ ratios of 1.7 and 2.4). If we suppose a higher excitation temperature than 30 K for these two clouds, it is possible to match the ProNaOS O&H values, for instance assuming $T \approx 80$ K leads to 10^{21} cm^{-2} for the ^{13}CO N_H value of Cloud 4, but this warm temperature is not likely for this region. Another possibility may be that the O&H opacity value still over-estimates the column density for these clouds, that may mean that they are the place of even more grain special effects than those taken into account by Ossenkopf & Henning.

We also show in Table 5 the mass of each region. This is obtained simply by multiplying the estimated gas column density by the surface of the region, assuming a distance of 470 pc.

For the clouds separated from the molecular complex, we may reasonably ask if they can collapse due to their mass and therefore become protostellar objects. As an indicator of the stability of the clouds, we give in Table 5 the Jeans mass. We use for this the expression derived

Table 5: Column densities estimated from the opacities of Désert *et al.* (90), Ossenkopf & H. (94), and from the ^{13}CO data of Nagahama *et al.* (98). Masses, Jeans mass, densities.

	N_H Désert	N_H Ossenkopf	N_H ^{13}CO	Mass Dés.	Mass Oss.	Jeans m.	Density Dés.	Density Oss.
	10^{20}cm^{-2}	10^{20}cm^{-2}	10^{20}cm^{-2}	(M_\odot)	(M_\odot)	(M_\odot)	(protons/ cm^3)	(protons/ cm^3)
OMC-1(3.6')	1400	—	1080	212	—	—	138000	—
ISF								
(south) 5.4'	245	—	270	83	—	—	16100	—
ISF								
(north) 4.2'	525	—	340	108	—	—	44400	—
Cloud1 (3.5')	320	115	175	42	15	12.6	33800	12200
Cloud2 (3.5')	320	120	100	46	17	8.7	32900	11900
Cloud3 (3.5')	95	34	20	9.9	3.6	8.4	11300	4070
Cloud4 (5.2')	33	12	5	10.3	3.7	18.5	2220	802

from the equality of gravitational and thermal energy (Larson 1969):

$$M_J = 10^{-18} \cdot \frac{D_{cm}}{2} \cdot T$$

with M_J in solar masses and D_{cm} the diameter in cm of the cloud.

T refers in this equation to the gas temperature, whereas we used the dust temperature found. In the dense interstellar medium, the two temperatures are weakly different (Hollenbach 1988, Tielens & Hollenbach 1985). We assume by this way that the mass is essentially the clump's one, and that the gas temperature of the clump is about the same as the dust one, but it may be different from the temperature of the supposed surrounding gas (traced by the ^{13}CO).

The comparison of the cloud mass to the Jeans mass is here to be taken as an indicator of the cloud's instability. There are of course large uncertainties in both the clump's measured mass and the non thermal sources of internal energy, such as magnetic field and turbulence, which can help to balance the gravitational energy. On the other hand, external pressure may lead to stabilization of otherwise evaporating clumps. In our sample of four cold clouds, there is a trend that the clumps closer to the active region (Clouds 1 and 2) are potentially the more unstable.

5. Conclusion and summary

Our study shows a large distribution of temperatures and spectral indexes in and around a dense and active molecular complex, the M42 Orion Nebula. The temperature varies from 12 K to 70 K, and the spectral index from 1.1 to 2.2. The finding of two new cold clouds (Clouds 3 and 4) confirms that the existence of cold condensations in such regions is not unusual. However the extended cold clumps are located in the outskirts of the active star forming area. They may be the sites for future star formation.

The statistical analysis of the temperature and spectral index spatial distribution shows an evidence for an inverse correlation between these two parameters. This effect is not well explained yet, especially in the submillimeter spectral range for cold grains (< 20 K). It has been shown

to occur in the laboratory for warm grains by Mennella *et al.* (1998), and for cold grains in the millimeter by Agladze *et al.* (1996).

We estimated the column densities and masses of the observed regions, by simply modelling the thermal emission of the grains from Désert *et al.* (1990) or Ossenkopf & Henning (1994). There is a good agreement between the ^{13}CO column densities and those derived from our submillimeter measurement. This demonstrates the robustness of dust opacity values in the grain models. The submillimeter wide band spectro-imaging is thus a natural way to derive masses in the interstellar medium.

Finally we see a trend that the closer to the complex the cold clouds are, the more unstable they are. The history of star formation around OMC-1 shows that there have already been 3 to 4 successive bursts of star formation in this region with the embedded cluster responsible for the BN/KL object being the latest. The clouds that we observe close to the active region may thus be the seeds of the next generation of stars. This is of course quite speculative and should be sustained by more observations, particularly of the possible embedded protostars.

6. Acknowledgements

We wish to thank Drs Nagahama, Mizuno, Ogawa and Fukui, for kindly having provided us their CO maps. We are indebted to the French space agency Centre National d'Études Spatiales (CNES), which supported the ProNaOS project. We are very grateful to the ProNaOS technical teams at the CNRS and CNES, and to the NASA-NSBF balloon-launching facilities group of Fort Sumner (New Mexico).

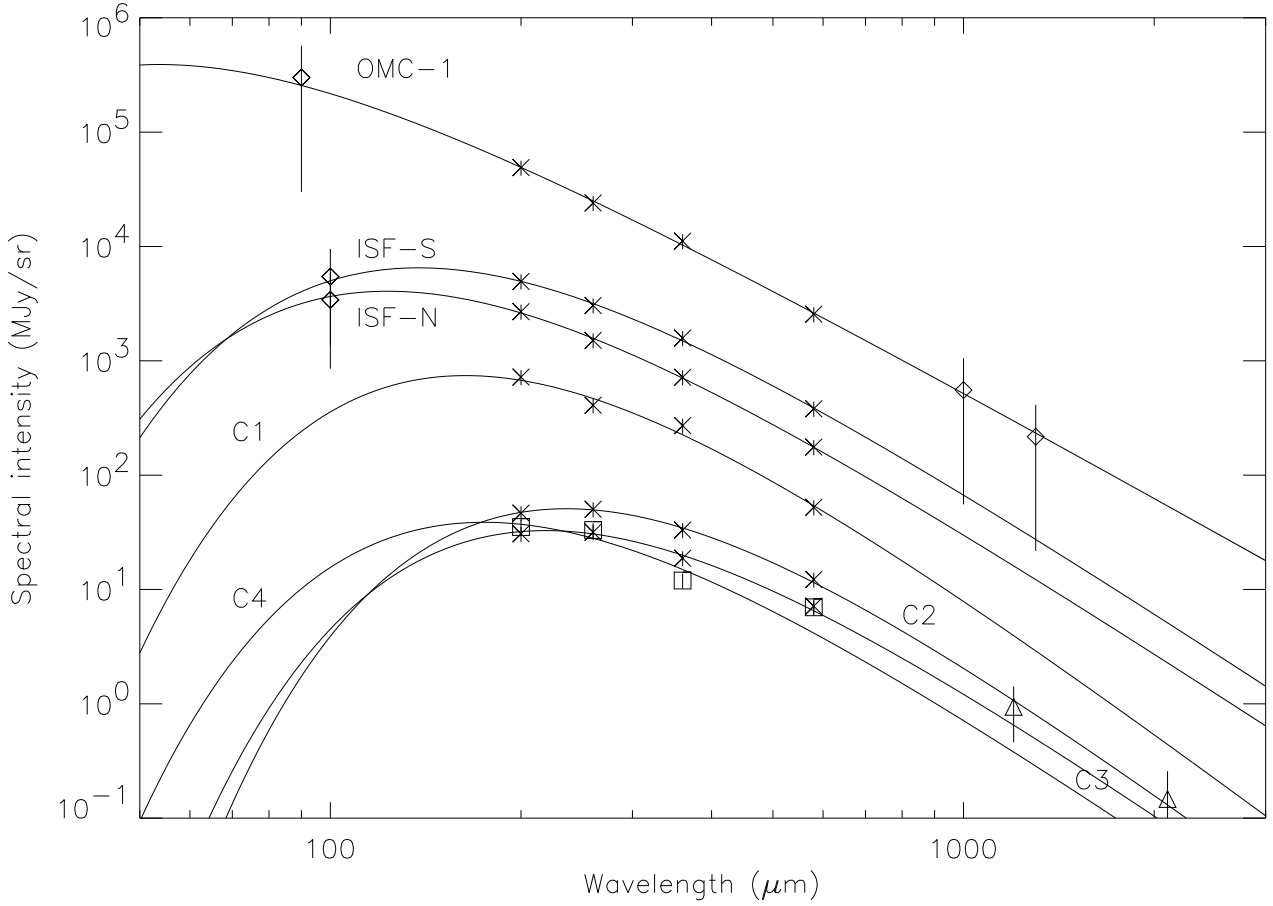


Fig. 3.— Spectra with 3σ error bars. The crosses stand for the ProNaOS points, the triangles for the DiaBolo points (Cloud 2), and the diamonds for the other data. For clarity, the Cloud 4 ProNaOS points appear as squares. The ProNaOS error bars are the intercalibration errors. The drawn lines are the result of the fits (modified black body).

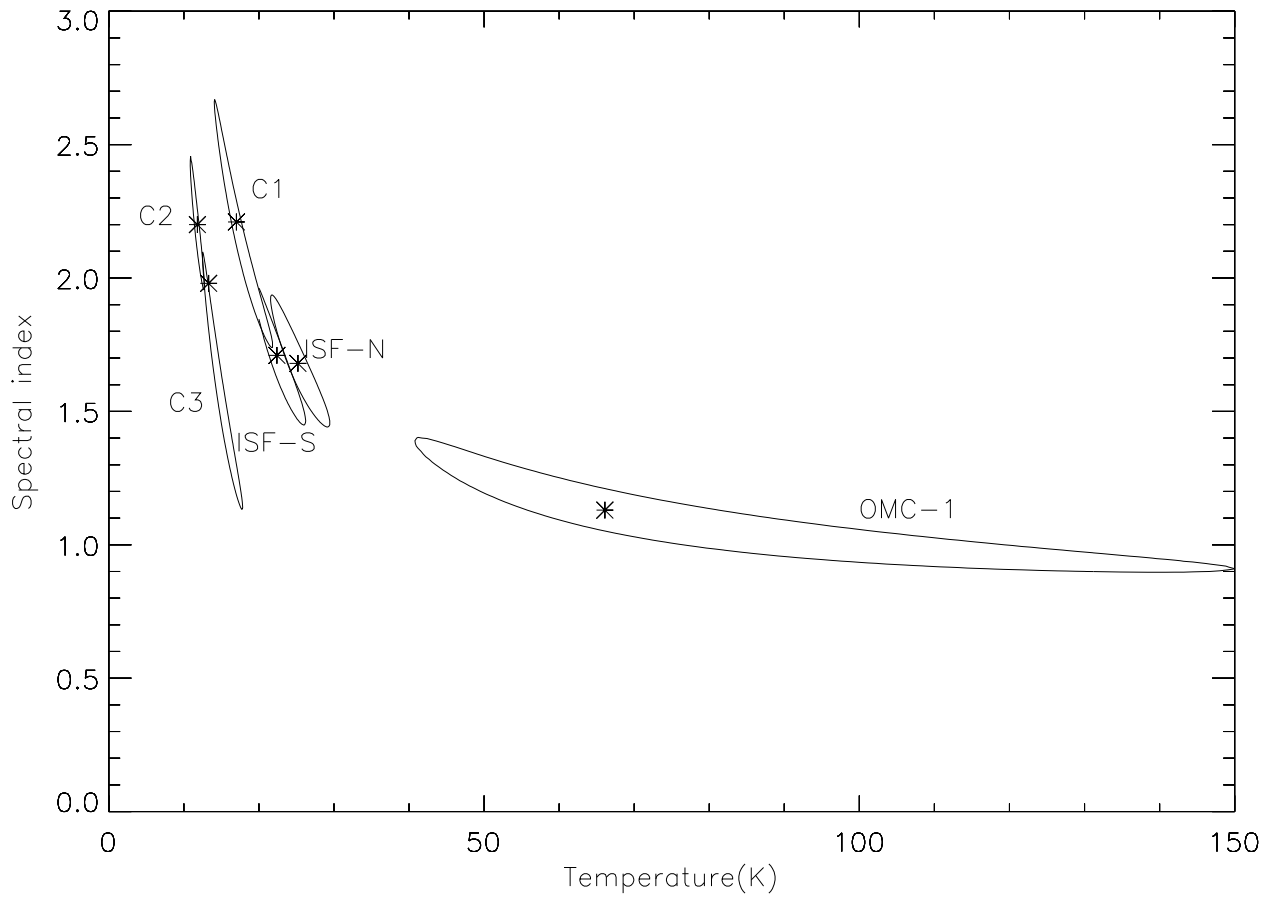


Fig. 4.— 1σ likelihood contours of six regions of M42. The drawn crosses are the positions of the maximum likelihoods.

REFERENCES

- Agladze, N.I., Sievers, A.J., Jones, S.A., Burlitch, J.M., Beckwith, S.V.W.: 1996, *ApJ*, 462: 1026-1040
- Bally, J., Stark, A.A., Wilson, R.W., Langer, W.D.: 1987, *ApJ*, 312L, 45B
- Bally, J., Langer, W.D., Liu, W.: 1991, *ApJ*, 383: 645-663
- Becklin, E.E., Neugebauer, G.: 1967, *ApJ*, 147: 799
- Benoît, A., *et al.* : 2000, *Astron. Astrophys. Suppl.*, 141: 523B
- Buisson, F., Duran, M.: 1990, *Proc. 29th Liège Colloq., ed. B. Kaldeich (Paris: ESA)*, 314
- Castets, A., Duvert, G., Dutrey, A., Bally, J., Langer, W.D., Wilson, R.W.: 1990, *A&A*, 234: 469-486
- Castets, A., Langer, W.D.: 1995, *A&A*, 294, 835C
- Chini, P., Creysa, E., Mezger, P.G., Gemund, H.P.: 1984, *A&A*, 137, 117
- Chini, R., *et al.* : 1997, *ApJ*, 474, L135
- Désert, F.-X., Boulanger, F., Puget, J.-L.: 1990, *A&A*, 237: 215-236
- Dupac, X., Giard, M., Bernard, J.-P., Lamarre, J.-M., Pajot, F., Ristorcelli, I., Serra, G., Torre, J.-P.: 2001, *From Darkness to Light, ASP Conference Series*
- Dutrey, A., Duvert, G., Castets, A., Langer, W.D., Bally, J., Wilson, R.W.: 1993, *A&A*, 270, 468D
- Emerson, D.T., Klein, U., Haslam, C.G.T.: 1979, *A&A*, 76, 92
- Franco, J, Tenorio-Tagle, G., Bodenheimer, P., Rozyczka, M., Mirabel, I.F.: 1988, *ApJ*, 333, 826
- Genzel, R., Stutzki, J.: 1989, *Ann. Rev. Astron. Ap.*, 27, 41

- Goldsmith, P.F., Bergin, E.A., Lin, D.C.: 1997, *ApJ*, 491, 615
- Goudis, C.: 1982, *The Orion complex, a case study of interstellar matter*, D. Reidel
- Harper, D.A.: 1974, *ApJ*, 192: 557-576
- Hillenbrand, L.: 1997, *Astron. J.*, 113, 1733
- Hollenbach, D.J.: 1988, *IAU Symp. on Interstellar Dust*
- Johnstone, D., Bally, J.: 1999, *ApJ*, 510: L49
- Käufel, H.U., Siebenmorgen, R.: 1995, *The role of dust in the formation of stars*, *Proc. ESO Workshop Garching*
- Kleinmann, D.E., Low, F.J.: 1967, *ApJ*, 149: L1
- Kutner, M.L., Tucker, K.D., Chin, G., Thaddeus, P.: 1977, *ApJ*, 215: 521-528
- Lamarre, J.M., *et al.* : 1994, *Infrared Phys. Tech.*, 35, 277
- Larson, R.B.: 1969, *MNRAS*, 145, 271
- Laureijs, R.J., Clark, F.O., Prusti, T.: 1991, *ApJ*, 372: 185
- Lis, D.C., Serabyn, E., Keene, J., Dowell, C.D., Benford, D.J., Phillips, T.G., Hunter, T.R., Wang, N.: 1998, *ApJ*, 509: 299
- Maddalena, R.J., Morris, M., Moscowitz, J., Thaddeus, P.: 1986, *ApJ*, 303: 375
- Mennella, V., Brucato, J.R., Colangeli, L., Palumbo, P., Rotundi, A., Bussoletti, E.: 1998, *ApJ*, 496: 1058
- Mezger, P.G., Wink, J.E., Zylka, R.: 1990, *A&A*, 228, 95
- Mookerjee, B., Ghosh, S.K., Rengarajan, T.N., Tandon, S.N., Verma, R.P.: 2000, *A&A*, 120, 1954M

- Nagahama, T., Mizuno, A., Ogawa, H., Fukui, Y.: 1998, *Astron. J.*, 116, 1, 336-348
- Ossenkopf, V., Henning, T.: 1994, *A&A*, 291: 943-959
- Ristorcelli, I.: 1995, *PhD thesis of the Université Paul Sabatier Toulouse III*
- Ristorcelli, I., De Luca, A., Giard, M., Pajot, F., Torre, J.-P., Serra, G., Lamarre, J.M.: 1995, *Proc. ESO Workshop Garching*
- Ristorcelli, I., Serra, G., Lamarre, J.M., Giard, M., Pajot, F., Bernard, J.-P., Torre, J.P., De Luca, A., Puget, J.L.: 1998, *ApJ*, 496: 267-273
- Ristorcelli, I., Serra, G., Lamarre, J.-M., Giard, M., Bernard, J.-P., Pajot, F., Torre, J.-P., Abergel, A., Lagache, G., Puget, J.-L.: 1998, *Les Houches Colloq.*
- Ristorcelli, I., *et al.* : 2001, *in preparation*
- Sales, N., Chabaud, J.-P., Giard, M., Brockman, B., Clavier, J.-P.: 1991, *Experimental Astron.*, 2, 1-26
- Tegmark, M.: 1997, *ApJ*, 480, L87
- Thronson, H.A. *et al.* : 1986, *Astron. J.*, 91: 1350-1356
- Tielens, A., Hollenbach, D.J.: 1985, *ApJ*, 291: 722-746
- Wiener, N.: 1949, *Extrapolation and Smoothing of Stationary Time Series*, NY: Wiley

This figure "dupac_orion_fig1.jpg" is available in "jpg" format from:

<http://arxiv.org/ps/astro-ph/0102407v1>

This figure "dupac_orion_fig2.jpg" is available in "jpg" format from:

<http://arxiv.org/ps/astro-ph/0102407v1>